Measurement of the UV Reflectivity of Aluminium in Different Stages of Oxidation

Sebastian Mann

Bachelorarbeit in Physik

vorgelegt der

Fakultät für Mathematik, Informatik und Naturwissenschaften der
Rheinisch-Westfälischen Technischen Hochschule Aachen

im September 2012

angefertigt am

III. Physikalischen Institut A

Gutachter und Betreuer

Prof. Dr. Thomas Hebbeker
III. Physikalisches Institut A
RWTH Aachen University

Abstract

This thesis examines the change of the reflectivity of an aluminium surface used for light concentrators at various stages of oxidation. The experimental setup consists of an LED in the UV regime as light source and a fibre spectrometer as detector. First, the light beam of the LED is measured by the detector fibre to get the intensity of the unreflected light beam. Secondly, an aluminium surface is positioned into the optical path, so that the intensity of the reflected beam can be measured for three different incident angles of 45°, 60° and 75°. The reflectivity as ratio of the two intensities is measured for different periods of oxidised aluminium. The oxid thickness on the aluminium surface does not influence the reflectivity in the UV regime of the aluminium surface, so that even after a long time use, the light concentrators in the FAMOUS telescope will not decrease in their efficiency.

Zusammenfassung

Diese Arbeit beschäftigt sich mit der Veränderung einer Aluminiumoberfläche, während die Oberfläche oxidiert. Der experimentelle Aufbau besteht aus einer LED, die im UV-Bereich leuchtet, als Lichtquelle und einer Detektionsfaser, die an ein Faserspektrometer gekoppelt ist. Zuerst wird der Lichtstrahl der LED durch die Detektionsfaser gemessen, um die Intensität des unreflektierten Lichtstrahls zu erhalten. Als zweites wird die Aluminiumoberfläche in den Strahlengang gebracht, um dann die Intensität des reflektierten Lichtstrahls zu messen. Dies geschieht für drei verschiedene Einfallswinkel 45°, 60° und 75°. Für verschieden lange Oxidationszeitspannen wird die Reflektivität als Verhältnis der beiden Intensitäten gemessen. Die Dicke der Oxidschicht hat jedoch keinen Einfluss auf die Reflektivität der Aluminiumoberfläche, sodass selbst nach einem langen Zeitraum die Effizienz der Lichtkonzentratoren im FAMOUS Teleskop nicht sinken wird.

Contents

List of Figures

Chapter 1

Motivation

Today, astrophysicists want to measure the flux of ultra high cosmic rays (UHECRs) as exact as possible, including their origin and chemical composition. These UHECRs are particles from space hitting the atmosphere of the Earth. For increasing energies of the UHECRs, their flux decreases and at energies above 10^{19} eV, only one particle per square kilometre and year is detected on the Earth. This requires experiments with a big exposure.

The Pierre Auger Observatory is a large array of Cherenkov detectors covering an instrumentation area of more than $3000\,\mathrm{km}^2$ by a surface detector. A fluorescence light detector consisting of 27 telescopes completes the detection instruments. A particle entering the atmosphere of Earth produces an avalanche of secondary particles (extensive air shower) which excite the nitrogen molecules of the atmosphere. These nitrogen molecules emit light in the ultraviolet regime as they deexcite, which is collected by the telescopes and measured with each 440 photomultiplier tubes arranged in a hexagonal grid.

The FAMOUS telescope is a project to use silicon photomultipliers (SiPMs) to detect the fluorescence photons of the extensive air showers. SiPMs have several advantages compared to conventional photomultipliers as they do not need a high voltage supply and promise a higher photon detection efficiency. FAMOUS is an acronym for "First Auger MPPC camera for the Observation of UHECR air Showers" and MPPC itself stands for "Multi-Pixel Photon Counter".
To increase the efficiency and reduce the dead space of the silicon photomultipliers in the focal plane, Winston cones made of polished aluminium are used as light funnels. With time, the aluminium surface starts to oxidise. Therefore, it is necessary to know, which are the deteriorations introduced to the reflection of the surface. The analysis of these is the main topic of this thesis.

Chapter 2

Introduction

The following chapter will shortly discuss the history of the research of cosmic rays, their characteristics and the methods of measurement and reconstruction of extensive air showers.

2.1 History of Cosmic Rays

In 1912, Victor Hess first discovered cosmic rays as he did several balloon ascends and studied the ionisation rate of the air as a function of the altitude [1]. Before 1912, radioactive materials of Earth were believed to be the origin of the radiation, but V. Hess measured an increase of the radiation as he moved higher into the sky. So he concluded the radiation to origin from outer space. In 1929, W. Bothe and W. Kolhörster found out that the cosmic radiation consists of charged particles. Kohlhörster studied the coincident signals between two Geiger Müller tubes and argued that the tubes measured secondary particles being produced by the same primary particles.
As further researches were limited by a low cosmic ray flux (particles per time and area), large sensitive areas and long exposure time, and consequently new detector techniques were needed. Thus, in the middle of the 1940s, large detector arrays on the ground of the Earth were installed using e.g. the atmosphere as a calorimeter to measure the extensive air showers - the beginning of the modern high energy cosmic ray experiments.

2.2 Energy Spectrum of Cosmic Rays

In the following decades, several experiments were done to measure the different particles of the cosmic rays in a vast energy range up to more than 10^{20} eV. The energy flux falls steeply as a power law with the energy decreasing from more than 1000 particles per second and square meter in the GeV region down to less than one particle per square kilometre and century above 100 EeV:

$$\frac{\mathrm{d}^4 n}{\mathrm{d}E \mathrm{d}t \mathrm{d}\Omega \mathrm{d}A} \propto E^{-\gamma} \tag{2.2.1}$$

with the number of particles n, the energy E, the solid angle Ω, the time t, the area A and the spectral index γ representing different values in different ranges of the energy spectrum. The spectrum is presented in figure 2.2.1. In a wide range of the spectrum up to primary energies of several PeV, known as the "knee", γ is equal to 2.7. At the "knee", the spectrum gets even steeper with γ changing to 3.1. At approximately $4 \cdot 10^{17}$ eV (the so called "second knee") the spectrum gets steeper and at $4 \cdot 10^{18}$ eV (the "ankle") it gets flatter again with $\gamma = 2.6$.

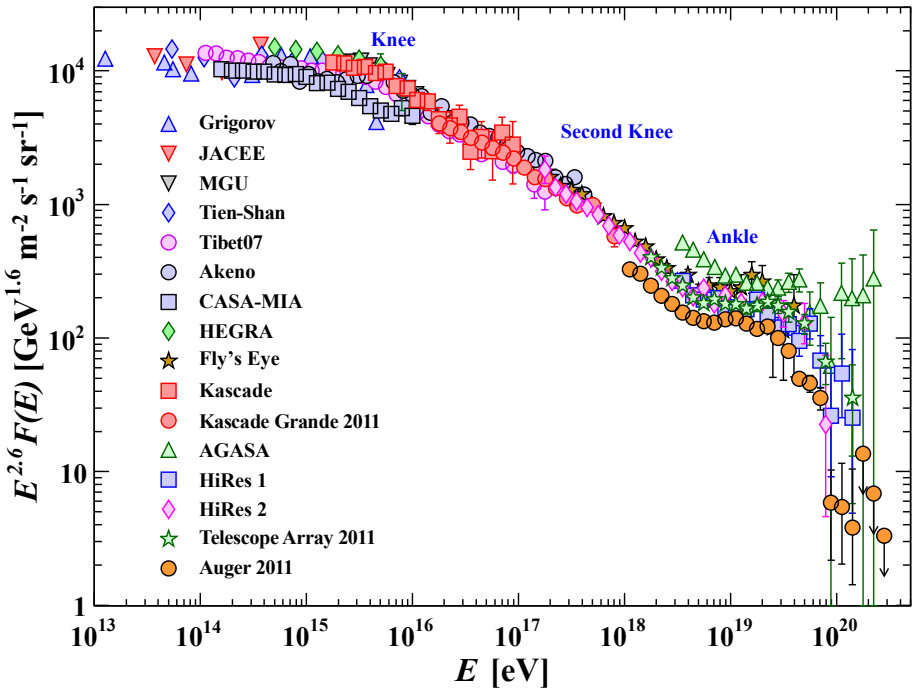

Figure 2.2.1: All-particle energy spectrum as obtained by measurements with different detectors. Taken from [2].

Understanding the knee is seen to be a big cornerstone of understanding the origin of cosmic rays. Thus, many approaches are currently discussed in the literature [1]. A popular explanation for the knee is based on the upper limit of acceleration by galactic supernovae. The ankle might be based on extragalactic particles which are less intense but dominate at higher energies. Also a leakage of particles from the galaxy could be a possible reason.

2.3 Extensive Air Showers

As an high energy cosmic ray enters the atmosphere of the Earth, an avalanche of secondary particles is produced. This phenomenon is referred to as extensive air shower.

There are several shower components. The electromagnetic shower component is induced by electrons or positrons causing bremsstrahlung or photons causing pair production of electrons or positrons. Hadron-initiated showers in opposition to electromagnetic showers also produce a significant myon component [1].
The total energy loss of the electrons can be gained via the formula

$$\frac{\mathrm{d}E}{\mathrm{d}X} = -\alpha(E) - \frac{E}{X_\mathrm{R}} \tag{2.3.1}$$

with the atmospheric depth X, the ionisation energy loss $\alpha(E)$ given by the Bethe-Bloch formula and the radiation length X_R which is $X_\mathrm{R} \approx 37\, g/cm^2$ for air [1].
A very simple model to understand the properties of electromagnetic showers is the Heitler model. Under the assumption that an incoming particle interacts in the atmosphere after a distance λ_em, it produces two new particles with each having half of the energy of the origin particle. This process proceeds until the new particles fall below a critical energy E_C, at which a particle loses the same energy due to ionisation and particle production. The maximum number of particles in a shower then is given by

$$N_\mathrm{max} = E_0/E_\mathrm{C} \tag{2.3.2}$$

and the depth of the shower maximum

$$X_\mathrm{max} = \lambda_\mathrm{em} \log_2(E_0/E_\mathrm{C}) \tag{2.3.3}$$

This model shows two important features: N_max at the shower maximum X_max is proportional to the energy of the primary particle which initiated the shower. Secondly, X_max increases logarithmically with increasing energy.
In 1977, Gaisser and Hillas proposed a function describing the longitudinal shower profile:

$$N(X) = N_\mathrm{max} \left(\frac{X - X_0}{X_\mathrm{max} - X_0} \right)^{(X_\mathrm{max} - X)/\lambda_\mathrm{int}} \exp\left(\frac{X_\mathrm{max} - X}{\lambda_\mathrm{int}} \right) \tag{2.3.4}$$

with the maximum number of particles N_max, the depth of the first interaction X_0, the depth of the shower maximum X_max and the mean interaction length λ_int [1]. For air the mean interaction length of a proton is

$$\lambda_{\mathrm{int,\ air}} = 80\, g\, cm^{-2} \tag{2.3.5}$$

2.4 Fluorescence Light

The charged particles of an extensive air shower excite the nitrogen molecules of the air [1]. These then emit fluorescence light as they change from an excited state to the ground state. The emitted spectrum in the ultraviolet regime can be seen in figure 2.4.1. The most prominent transition is at 333 nm.

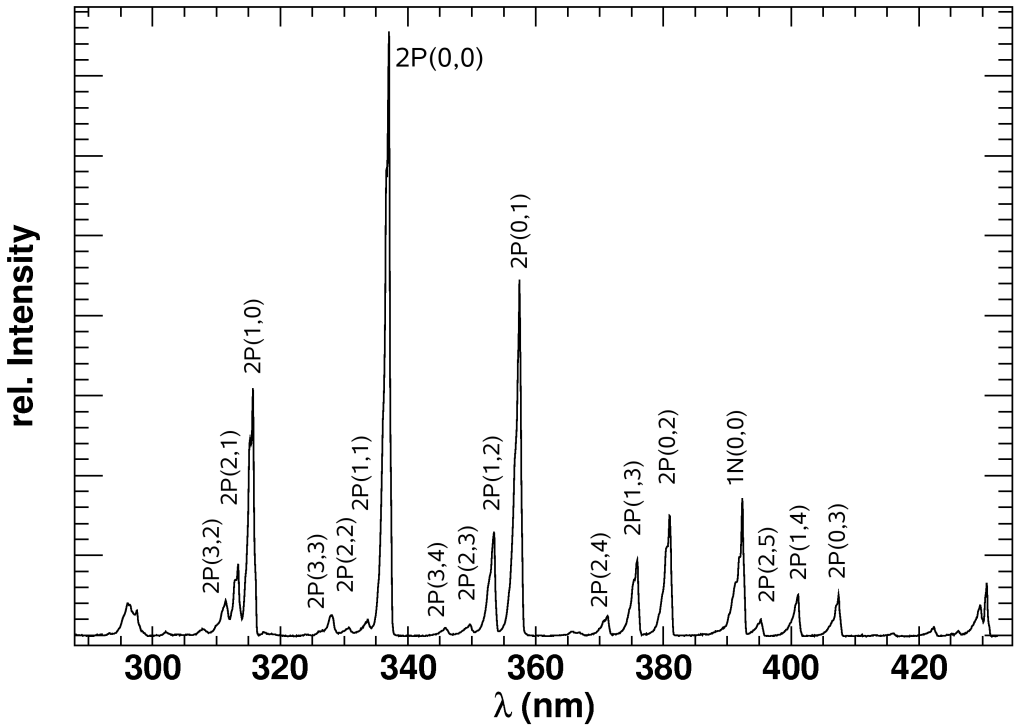

Figure 2.4.1: Fluorescence light spectrum of molecular nitrogen. It was measured by the AIRFLY experiment with an electron beam at 3 MeV at 20° C and 800 hPa. The transitions of the term scheme of nitrogen are named. Taken from [3] [4].

The number of fluorescence photons N_γ^0 is proportional to the energy deposit per traversed matter $\mathrm{d}E_{\mathrm{dep}}^{\mathrm{tot}}/\mathrm{d}X$:

$$\frac{\mathrm{d}^2 N_\gamma^0}{\mathrm{d}X\mathrm{d}\lambda} = Y_\lambda(\lambda, P, T, u) \cdot \frac{\mathrm{d}E_{\mathrm{dep}}^{\mathrm{tot}}}{\mathrm{d}X} \quad . \tag{2.4.1}$$

The proportionality constant Y_λ is referred to as the fluorescence yield. It depends on the wavelength λ, the air pressure P, the temperature T and the humidity u but is independent of the energy of the exciting particle as measurements confirm [5].
The fluorescence light can be used to completely reconstruct the shower profile. Additionally, the profile reconstruction requires the determination of the geometry of the shower axis and the atmospheric absorption which is wavelength dependent [1]. Thus, it is necessary to continuously monitor the atmospheric conditions e.g. cloud coverage and abundance of aerosols. The accuracy can be improved by using more than one telescope at a time to measure the shower profile. A sketch of a geometry reconstruction can be seen in figure 2.4.2. The timing information t_i, when a detector pixel i receives a signal, can be used to fit the shower axis:

$$t(\chi) = t_0 + \frac{R_{\mathrm{p}}}{c} \tan[(\chi_0 - \chi)/2] \tag{2.4.2}$$

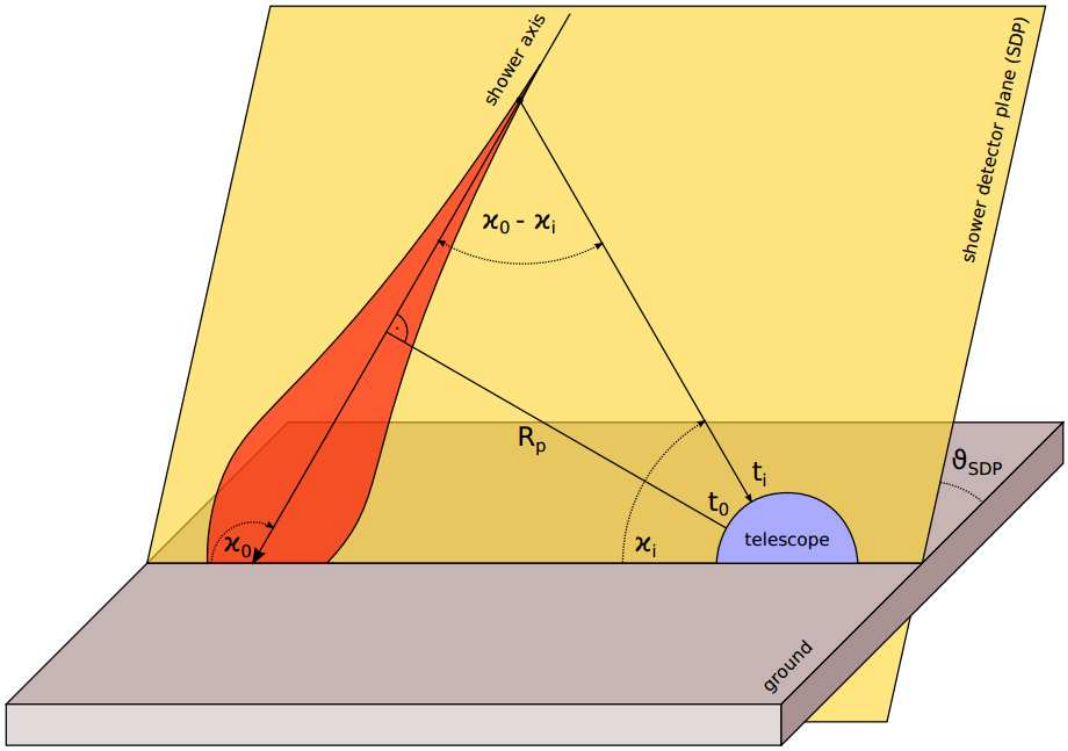

Figure 2.4.2: Sketch of the shower-detector-plane. A signal S_i arrives at the telescope at a time t_i and under an angle χ_i. R_P is the shortest distance between the telescope and the shower axis. It is detected at $t = t_0$. Taken from [6].

2.5 FAMOUS

FAMOUS is an acronym for "First Auger Multi-Pixel Photon Counter camera for the Observation of Ultra high energy cosmic ray air Showers". It is a prototype telescope project with a refractive optic and will use silicon photomultipliers (SiPMs) to measure the fluorescence light of extensive air showers [5].

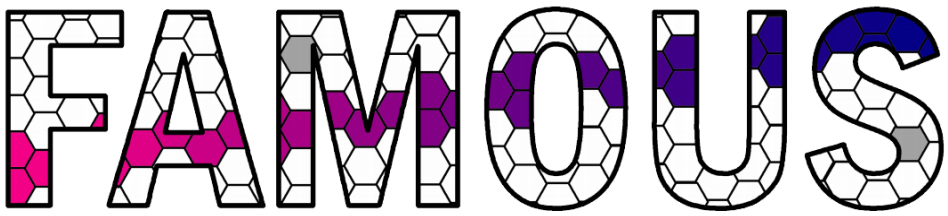

Figure 2.5.1: The logo of FAMOUS. FAMOUS is an acronym for "First Auger MPPC camera for the Observation of UHECR air Showers"

A screenshot of the Geant4[1] simulation of the telescope is presented in figure 2.5.2. As the refracting element, a Fresnel lens (diameter D = focal length f = 510 mm) is used since it has less weight and a lower absorption coefficient than a conventional lens and

[1] Geant4 is a software framework to simulate particles traversing matter.

can be produced cost efficient from UV-transparent acrylic [7]. The focal plane consists of 64 pixels each instrumented by four squared 3x3 mm^2 silicon photomultipliers (Hamamatsu s10985-100C). The pixels are arranged in a hexagonal structure. Winston cones work as light funnels to reduce dead space between the single SiPMs and thus increase the efficiency of the detector. The length of the Winston cone is 19.6 mm, the entrance radius is 6.7 mm and the exit radius is 3 mm to reach an area enlargement factor of 5.

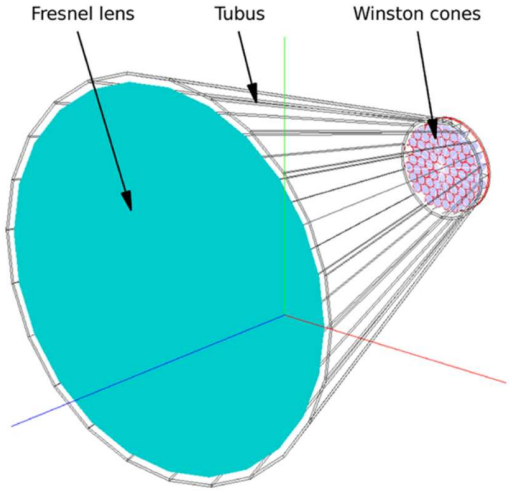

Figure 2.5.2: Screenshot of the Geant4 simulation of FAMOUS showing the setup of the telescope. A Fresnel lens (diameter D = focal lens f = 510 mm) focusses the light onto the focal plane which consists of hexagonally arranged Winston cones (entrance radius = 6.7 mm and exit radius = 3 mm) and SiPMs (each 6x6 mm^2). Taken from [7].

2.5.1 Silicon Photomultipliers

Silicon photomultipliers (SiPMs) are photodiodes allowing the detection of single photons with a time resolution of about 50 ps [7]. They consist of arrays of Geiger-mode avalanche photodiodes (G-APDs). If an incoming photon is absorbed, an electron-hole-pair is created and then accelerated by the applied electric field of the depletion zone of the diode junction. Impact ionisation creates more electron-hole pairs. Thereby, a current can flow so that the voltage drops. This is the signal for having registered the incoming photon (c.f. middle of figure 2.5.3). The avalanche is stopped by a so called quenching resistor.
As the signal is not proportional to the number of photons N_γ for a single G-APD, multiple G-APDs are arranged in arrays on an SiPM, so that the output signal is proportional to the detected number of photons again if the light is distributed homogeneously.
The photon detection efficiency (PDE) depends on the geometrical fill factor f_{geom} (dead space reduces the efficiency), on the quantum efficiency QE (probability for an incoming photon creating an electron-hole-pair) and on the trigger probability P_{trigger} (the probability that electron-hole-pairs cause an avalanche):

$$PDE = QE \cdot f_{\text{geom}} \cdot P_{\text{trigger}}. \tag{2.5.1}$$

In figure 2.5.3 a photography of an SiPM is shown (left). On the right side of the figure, a so called finger spectrum can be seen. The first peak (shifted to 10 because of an additional internal pedestal of the QDC) refers to the pedestal, where the SiPM did not detect any photons. The further peaks refer to the detection of one photon-equivalent (the second peak labelled as 1 p.e.), two photon-equivalents and so on. These peaks refer to the negative peaks shown on the oscilloscope screenshot in the middle of figure 2.5.3.

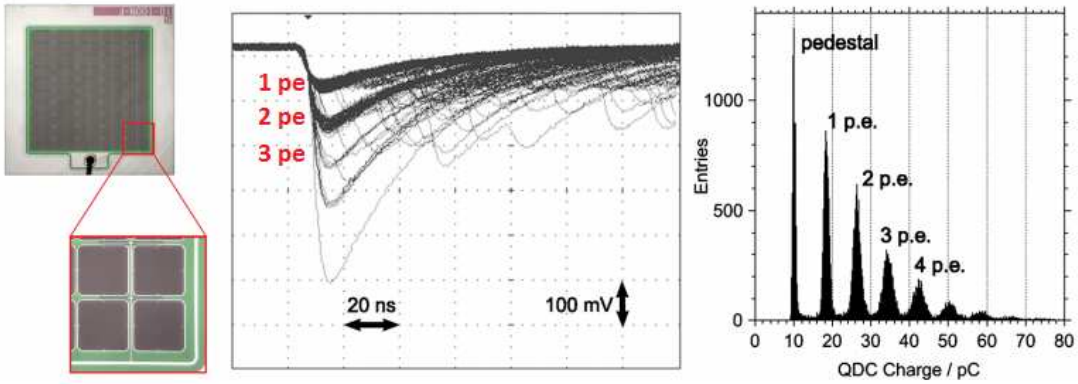

Figure 2.5.3: Left: Photography of a SiPM, **Middle:** Oscilloscope screenshot of cell triggers, **Right:** Measured charged spectrum of an SiPM. The frequency of the different p.e. are plotted against the deposited charge. Taken from [7].

There are different possibilities which can cause an avalanche process. Thermally induced breakdowns (strong thermal dependency so that either the temperature or the overvoltage[2] of the SiPM has to stay constant) as well as optical crosstalk between single G-APDs (electrons and holes recombine emitting an photon during an avalanche process) and afterpulsing (impurities in the silicon trap the electrons and release them after a while) can cause a signal [7].
The effects of correlated noise (crosstalk and afterpulsing) can be compensated by a descent analysis. More information can be obtained in [8].

2.5.2 Winston Cones

Winston cones are light funnels. They are needed to decrease dead space between the single SiPMs in the telescope FAMOUS and thus increase the effective sensitive area of an SiPM. This increases the detector efficiency. A cross section through a Winston cone is presented in figure 2.5.4 (left). It has a parabolic form and is symmetric with respect to the optical axis (red line). The two radii r_1 and r_2 are the entrance and exit radius of the cone. The exit radius is chosen to be 3 mm as the mounted array of four SiPMs (Hamamatsu s10985-100C) on the exit of the cone has got an area of 6x6 mm^2.

[2] The overvoltage U_{over} is defined as $U_{\text{over}} = U_{\text{bias}} - U_{\text{bd}}$ with the bias-voltage U_{bias} and the breakdown-voltage U_{bd}.

The entrance radius is $6.7\,\mathrm{mm}^2$ and results in an area enlargement of a factor of five. All light, that enters the Winston cone on the top under an angle

$$\theta_{\max} = arcsin\left(\frac{r_2}{r_1}\right) \approx 26^\circ \tag{2.5.2}$$

or a smaller angle, is reflected towards the exit of the cone. All other light beams are reflected back towards the entrance of the cone.

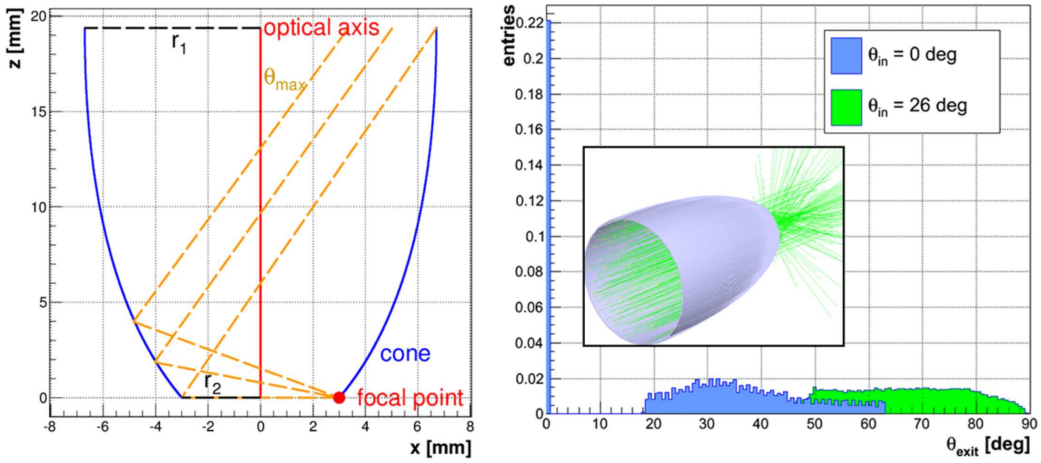

Figure 2.5.4: Left: Cross section through a Winston cone. The orange, dashed lines are light beams entering the cone on the top and leaving on the bottom. The blue lines show the parabolic form of the cone and the red line the optical axis which is at the same time the rotational axis of symmetry. **Right:** Simulation of a parallel light beam entering the Winston cone. For $\theta_{\text{in}} = 0^\circ$ and $\theta_{\text{in}} = 26^\circ$ the simulated distribution for θ_{out} is presented. Taken from [7].

The simulated distribution of the emergent angle for an incidence angle is presented in the right part of figure 2.5.4. Whereas for $\theta_{\text{in}} = 0^\circ$ about 25% directly pass through the cone without hitting the surface of the cone at all, 75% are scattered to a wide range of possible angles θ_{out}, for $\theta_{\text{in}} = 26^\circ$ all light beams are scattered [7]. The efficiency of the SiPM as a function of the incidence angle of light is analysed in the bachelor thesis of Daniel Wilson [9].

The simulated distribution for θ_{out} underlies spike reflection for a perfect surface. Impurities in the material lead to different kinds of reflection. The topic of this thesis will be to analyse the reflectivity for aluminium by changing different parameters like the incident angle of the light or the stage of oxidation. A detailed discussion of the characteristics of the aluminium and the different kinds of reflectivity of impure surfaces will be discussed in the next chapter.

Chapter 3

Reflectivity of Aluminium

This chapter will discuss the optical characteristics of aluminium concerning its properties of reflection. Therefore, different kinds of reflection mechanisms are explained.

3.1 Refractive Index of Aluminium

The refractive index describes the change of the phase velocity of electromagnetic waves, e.g. light, in matter compared to the one in vacuum [10]

$$n = \frac{c}{c'} \tag{3.1.1}$$

with the speed of light in the vacuum c and the speed of light in matter c'. Additionally, the velocity of propagation c' does not only depend on the matter the light traverses but also on the wavelength:

$$c' = c'(\lambda) \Rightarrow n = n(\lambda) \quad . \tag{3.1.2}$$

This dependence of this velocity of propagation c' on the wavelength λ is called dispersion. The refractive index consists of two fractions, a real part n and an imaginary part κ, which is responsible for absorption processes in matter. Both, the real and the complex part of the refractive index of aluminium, are presented in figure 3.1.1. The refractive index of aluminium for a wavelength of 400 nm is

$$\tilde{n} = n + i\kappa = 0.4879 + 4.8355i \quad . \tag{3.1.3}$$

For aluminium, the complex part dominates the absolute value of the refractive index and is responsible for the high reflection properties as the skin depth is in the magnitude of the wavelength.

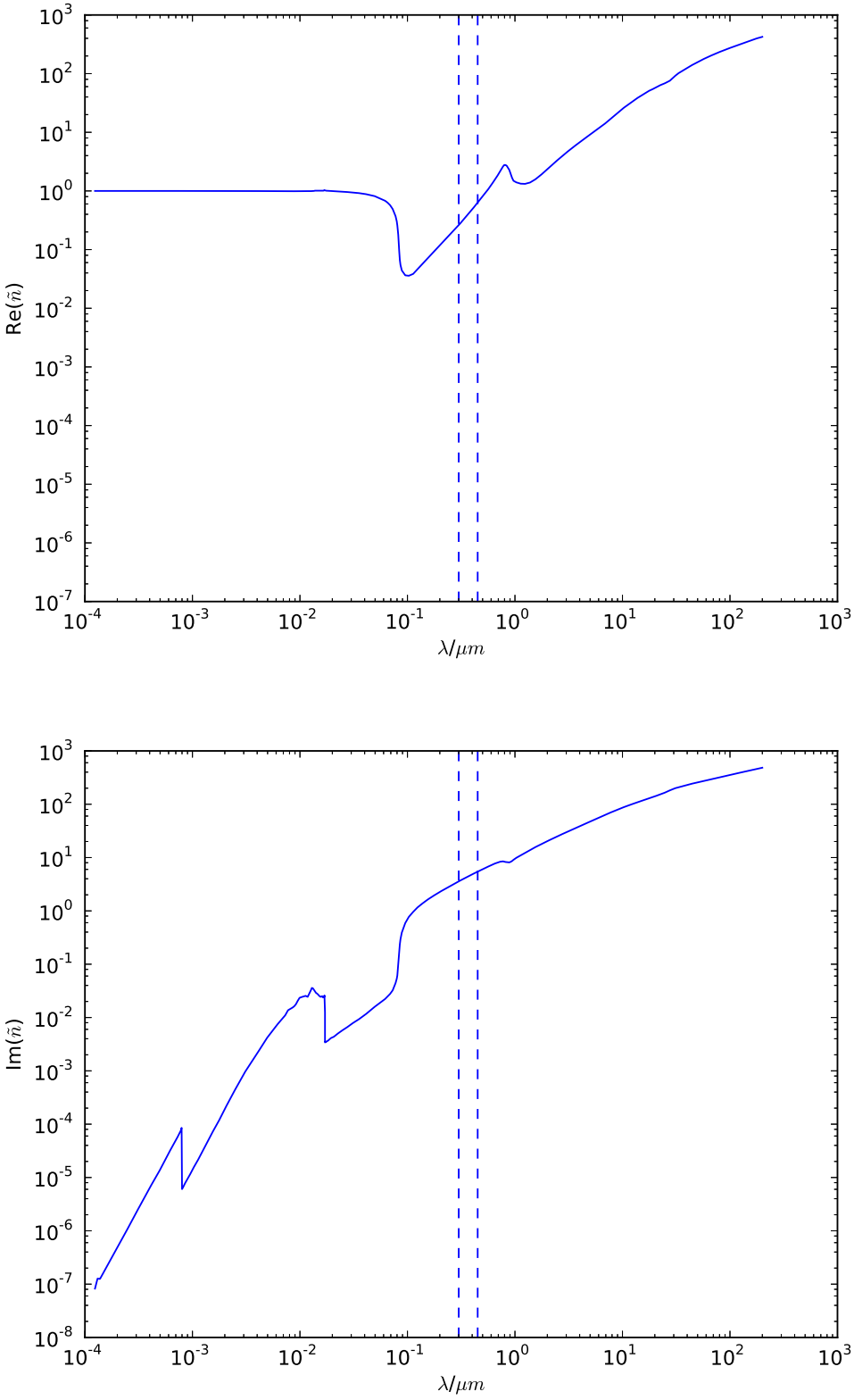

Figure 3.1.1: The reflective index of aluminium: On the top plot the real part, on the bottom plot the complex part versus the wavelength is shown. The dashed lines mark the ultraviolet regime between 300 nm and 450 nm. The axes are both logarithmically scaled and the wavelength is given in μm. Data taken from [11].

3.2 Stages of Oxidation

Aluminium surfaces oxidise during time, when the surface is exposed to air [12][13]. This additional coating can reduce the reflectivity of the surface. Therefore it is necessary to measure the reflectivity after definite periods of time to quantify change.
At first, a reflectivity measurement of a fresh polished aluminium surface is recorded. More measurements were performed for oxidation periods of two days, twelve days and twenty days. At last, after the last measurement of 20 days, the oxidation layer should be saturated and no longer increase in thickness.

3.3 Spike Reflection

The reflectivity of a material is described by the Fresnel equations [14]. They describe the behaviour of electromagnetic waves for the specific case of plane waves hitting a plane interface consisting of two different isotropic and homogeneous media. The Fresnel equations are derived directly from Maxwell's equations and depend on the incident angle of the light, on the refractive index and thus also on the wavelength.
It has to be distinguished between two different cases of polarised light. S-polarised light is the component of the light, that is perpendicularly to the plane of incidence, whereas p-polarised light corresponds to the parallel component with respect to the plane of incidence.
For s-polarised light, the reflectivity is given by

$$R_\mathrm{s} = \left| \frac{\tilde{n}_1 \cos\theta_\mathrm{i} - \tilde{n}_2 \sqrt{1 - \left(\frac{\tilde{n}_1}{\tilde{n}_2} \sin\theta_\mathrm{i}\right)^2}}{\tilde{n}_1 \cos\theta_\mathrm{i} + \tilde{n}_2 \sqrt{1 - \left(\frac{\tilde{n}_1}{\tilde{n}_2} \sin\theta_\mathrm{i}\right)^2}} \right|^2 \tag{3.3.1}$$

and for p-polarised light, by

$$R_\mathrm{p} = \left| \frac{\tilde{n}_1 \sqrt{1 - \left(\frac{\tilde{n}_1}{\tilde{n}_2} \sin\theta_\mathrm{i}\right)^2} - \tilde{n}_2 \cos\theta_\mathrm{i}}{\tilde{n}_1 \sqrt{1 - \left(\frac{\tilde{n}_1}{\tilde{n}_2} \sin\theta_\mathrm{i}\right)^2} + \tilde{n}_2 \cos\theta_\mathrm{i}} \right|^2 \tag{3.3.2}$$

with the incident angle Θ_i and the two refractive indices $\tilde{n}_1$ for the first medium (e.g. air) and $\tilde{n}_2$ for the second medium (e.g. aluminium).

The light of an Light Emitting Diode (LED) is unpolarised by definition [15] and thus the means reflectivity is given by

$$R = \frac{R_\mathrm{s} + R_\mathrm{p}}{2} \quad . \tag{3.3.3}$$

The reflectivity for $\tilde{n} = 0.4879 + 4.8355i$ and $\lambda = 400\,nm$ is plotted in figure 3.3.1. Both, s- and p-polarised light, as well as unpolarised light is plotted. The dependence on the wavelength is clearly visible. It has got a minimum around 75°.

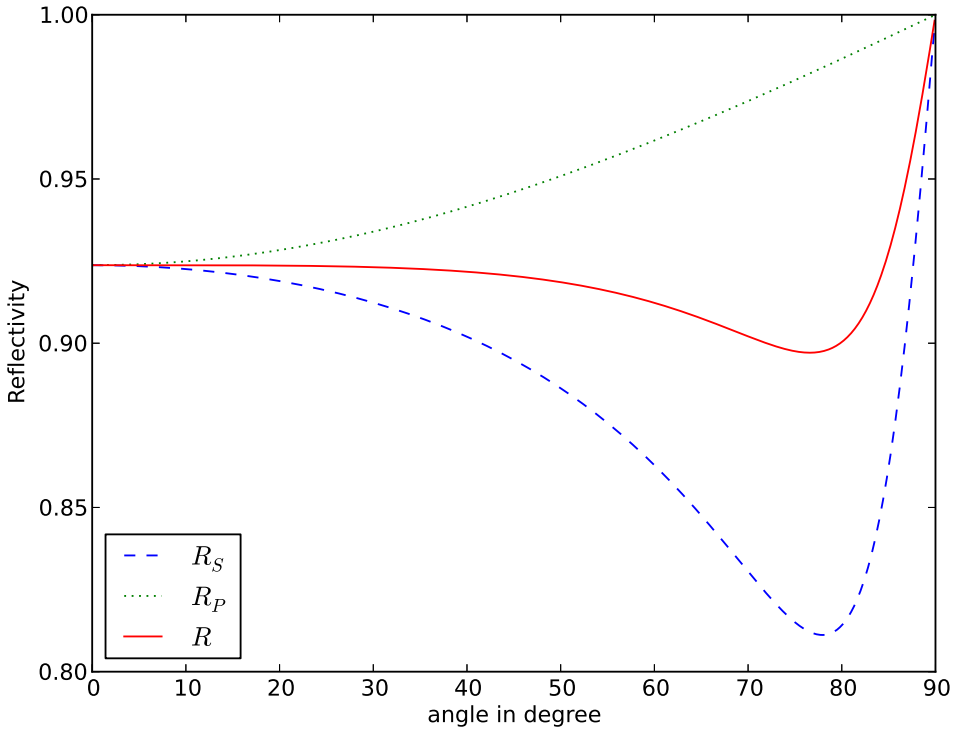

Figure 3.3.1: Reflectivity for aluminium with a refractive index of $\tilde{n} = 0.4879 + 4.8355i$ at $\lambda = 400\,nm$. Both, s- (dashed blue line) and p-polarised light (dotted green line), as well as unpolarised light (red continuous line) is presented.

3.4 Diffuse Reflection Phenomena

For spike reflection the surface of interface is assumed to be perfectly planar and thus a reflected photon is reflected described by the law of reflection in the same way it would be reflected by a perfect mirror [16].
In comparison to that, there are some more kinds of reflection that contain the fact, that the surface of an interface is not perfectly plane.

3.4.1 Backscatter Reflection

For backscatter reflection, a photon is reflected back to the direction where it came from [16] Examples are Compton scattering used in backscatter X-ray or alpenglow.

3.4.2 Lobe Reflection

Lobe reflection assumes the surface to consist of micro-facets, which are microscopic small surfaces [16]. These are tilted randomly with respect to the average macro-surface normal according to a Gaussian distribution:

$$f(\alpha) = \frac{1}{\sqrt{2\pi}\sigma_\alpha} \cdot \exp\left(-\frac{\alpha^2}{2\sigma_\alpha^2}\right) \quad . \tag{3.4.1}$$

A scetch of a micro-facet surface is presented in figure 3.4.1. The standard deviation of the Gaussian distribution is given by the parameter σ_α.

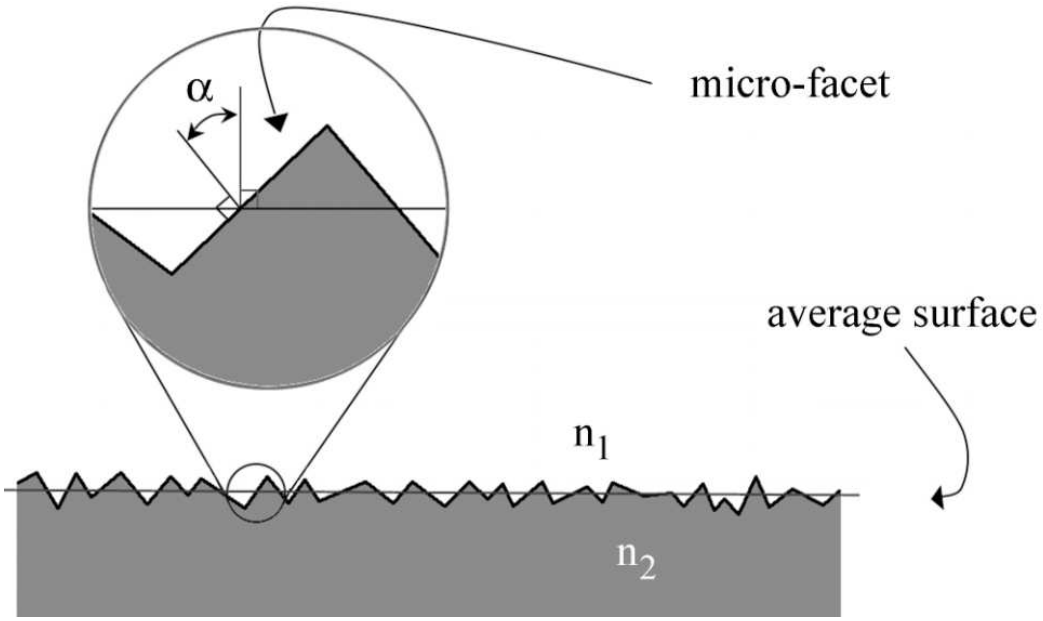

Figure 3.4.1: The surface consists of many small micro-facets on the average surface. The standard deviation of the Gaussian distribution is given by the parameter σ_α. Taken from [16].

3.4.3 Lambertian Reflection

For Lambertian reflection, the incoming photon will be reflected according to Lambert's Cosine Law [16]. This means the intensity distribution of the reflected photons is proportional to the cosine of the angle:

$$I(\theta) = const \cdot \cos(\theta). \tag{3.4.2}$$

The different kinds of reflection are presented in figure 3.4.2.

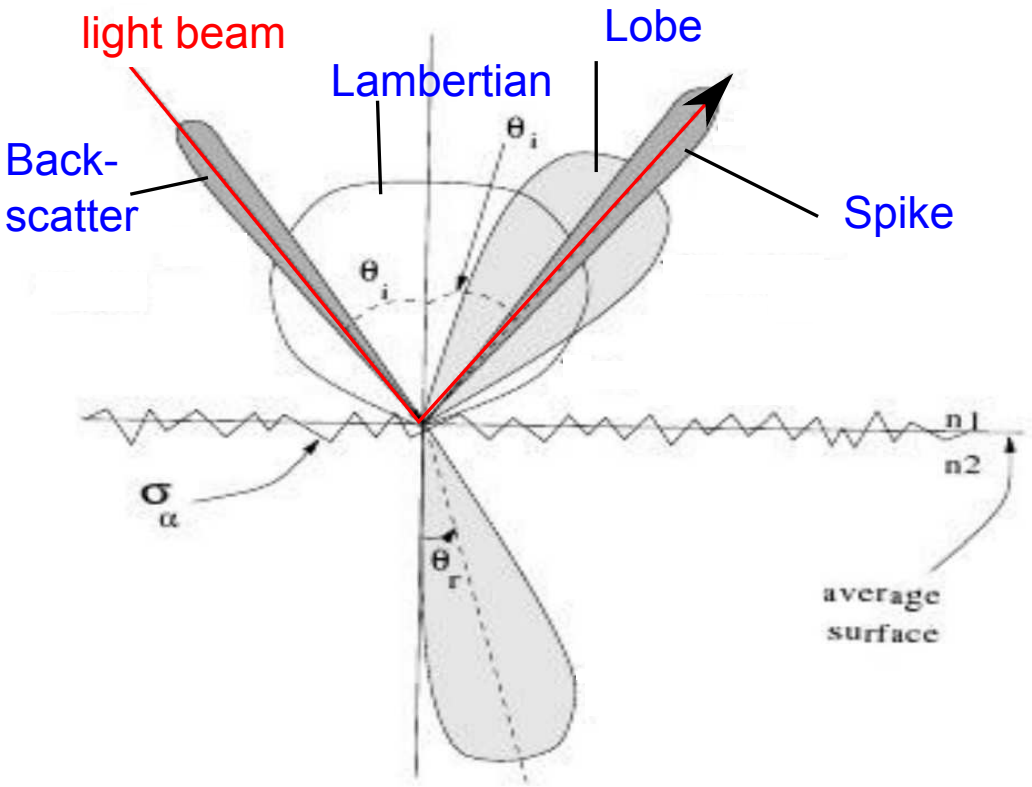

Figure 3.4.2: The different kinds of reflection -spike, backscatter, lobe and Lambertian reflection are presented with their typical directional characteristics. Taken from [17]

Chapter 4

Experimental Setup

In this chapter, the general setup of the experiment is presented and the different components used in the construction are explained.

4.1 Idea

The general idea about this setup is to measure first the light of an unreflected beam and secondly, the light being reflected by the aluminium surface exiting the aperture of a collimation tube. Then, the reflectivity is given by

$$R = \frac{I_{\text{refl}}}{I_{\text{beam}}} \tag{4.1.1}$$

with the intensity of the reflected beam I_{refl} and the intensity of the unreflected beam I_{beam}.
As the light beam is extensive after leaving the aperture, the detector has to cover an area greater than its sensitive area. Therefore a stepper moves the fibre, which is the detector, a fixed distance Δx, so that after each step the detector can measure the incoming flux of the light beam at a certain point. A sketch of the measurement is presented in figure 4.1.1.

Integration over all measurement points leads to a total intensity, which is necessary for getting the reflectivity (c.f. equation 4.1.1).

4.2 Layout Description

A photograph of the experimental setup is presented in figure 4.2.1. The light source is an LED in the UV regime around 400 nm and is located in (1). To get the light, which leaves the LED not as a parallel light beam, as best collimated as possible, it is conducted by a fibre-optic light guide to a collimation tube with a pin-hole aperture (2). The light exiting the aperture hits the aluminium cube and is reflected according to the Fresnel equations and strikes towards another fibre-optic light guide.

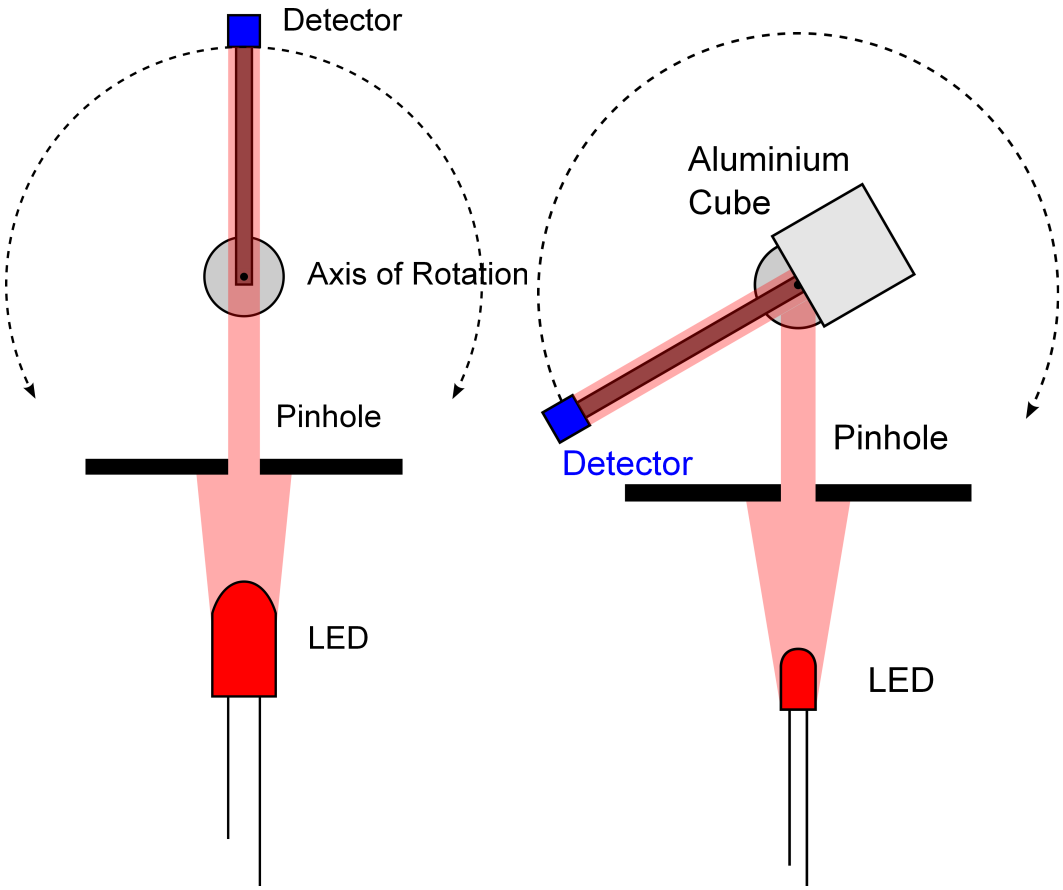

Figure 4.1.1: Sketch of the idea of the setup: **Left:** A sketch of the idea of the measurement of the lightbeam. **Right:** Now the aluminium surface is positioned in the optical path and the detector can measure the intensity of the reflected beam.

The fibre leads the detected light to a fibre spectrometer (5). The gained information on the intensity can be read out by a computer via the USB-port. An Arduino microcontroller (6) is used to steer the whole measurement as it applies voltage to the light source, the fibre spectrometer and to the stepper (not visible due to the fact that it is located underneath the aluminium cube). The whole setup is put into a dark box to minimize the pollution of the measurement by ambient light.

4.3 Fibre Spectrometer

The USB2000UV fibre spectrometer by Ocean Optics is used in this experiment as a light detector [18]. The detection technique of the spectrometer is presented in figure 4.3.1. The light enters the spectrometer through a fiber (1). An aperture slit regulates the incoming light flux (2) and a wavelength-dependent filter (3) lets only pass light in a range of 200 nm to 850 nm [18]. A mirror (4) collimates the light to a grating (5) which diffracts the light wavelength-dependent (with a resolution only limited by the size of the single pixels) to another mirror (6). After passing a collection lens, the light

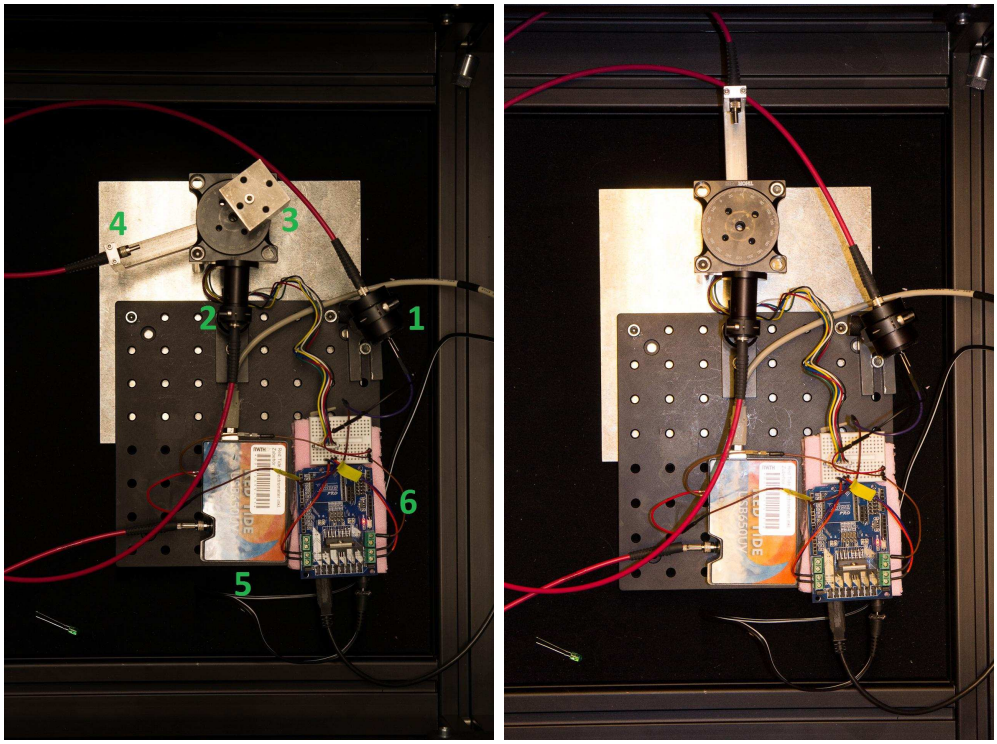

Figure 4.2.1: Left: The experimental setup is presented: (1) LED source, (2) collimation tube, (3) the aluminium cube, (4) the detection fibre connected to a stepper (not visible as underneath the aluminium cube), (5) the fibre spectrometer, (6) the Arduino board, **Right:** The same setup just without the aluminium cube. Necessary to measure the total beam intensity.

hits the CCD sensor, which consists of 2048 pixels each sized $14\mu m$ x $200\mu m$.

The sensitivity of the spectrometer is given by a signal-to-noise ratio of 250:1 (at full signal), stray light $< 0.10\%$ at 435 nm and an estimated sensitivity for each pixel of 90 photons per count at 400 nm. A linear calibration of the wavelength is accurate to 99.8%. The integrated memory is able to safe full scans every 13 milliseconds.

In front of the spectrometer a 10-pin connector is located [18]. The pin configuration can be seen in figure 4.3.2. Important for this experimental setup are the pins 6 and 7. Pin 7 can receive an external 5 V trigger signal, which the spectrometer can process, and pin 6 is the ground pin.

To read out the data from the spectrometer, the commercial software Spectrasuite is used. Spectrasuite is able to visualise and automatically safe a recorded spectrum onto the hard disk, after a trigger signal was registered. The spectrometer integrates the incoming light for 50 ms and assigns a count number of incoming photons to each wavelength. One count corresponds to 90 incoming photons. An upper limit of the detector is given by the saturation of 4096 counts per wavelength channel. Thus, it is possible to use Spectrasuite in combination with the Arduino to completely automatically record a whole measurement.

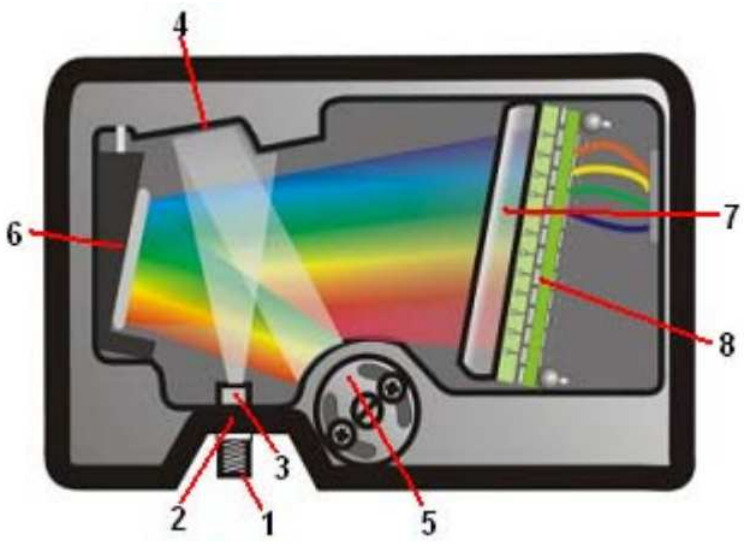

Figure 4.3.1: The detection technique of the fibre spectrometer: The light enters the spectrometer through a fibre (1), passes through an aperture slit (2) and a wavelength-dependent filter (3). A mirror (4) collimates the light to grating (5) which diffracts the light onto the focussing mirror (6) and a collection lens (7) so that the CCD sensor (8) can detect the wavelength-split light. Taken from [18] (figure 2-1).

10	8	6	4	2
9	7	5	3	1

Figure 4.3.2: 10-Pin Accessory Connector Pinout Diagram. The important pins are 6 (ground) and 7 (external trigger).

4.4 Light Source

The spectrum of the used LED is presented in figure 4.4.1. The LED has a distinctive peak around 400 nm, so that for further analysis a range between 387 nm and 411 nm can be used to determine the reflectivity. This range is illustrated by the two dashed lines.

Since the LED is not a point source, the light beam is expanded and has to be collimated. First, the light is send through a fibre. To make the light beam parallel best as possible, it is collimated by a pin-hole aperture after leaving the fibre, so that, after leaving the collimation tube the light beam only has got an extensive diameter of about 2 mm at the detector, which is nearly parallel and has virtually no angular divergence any more.

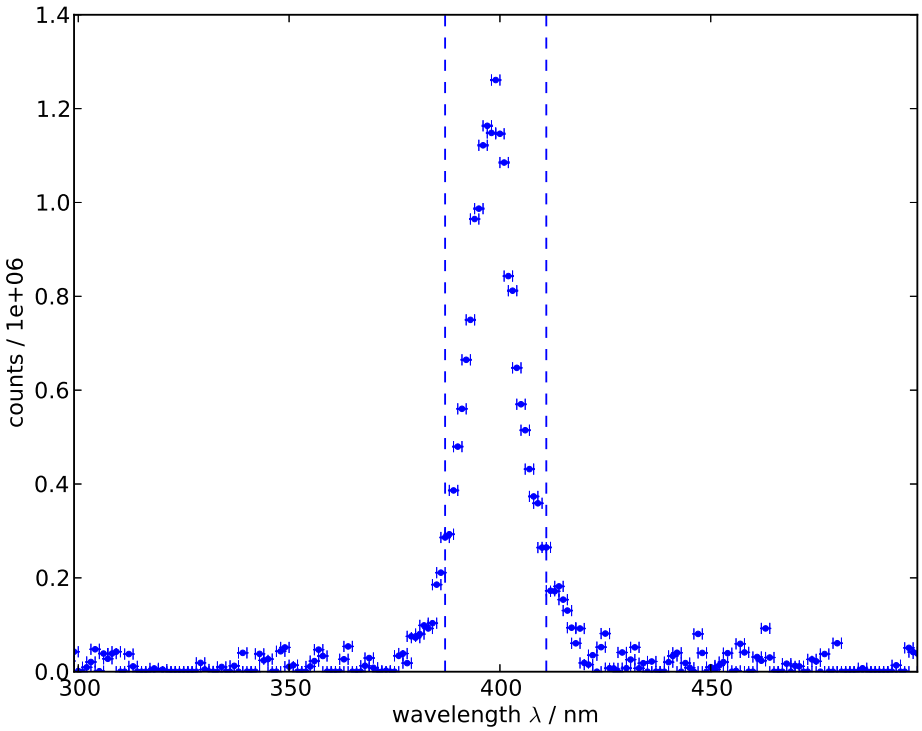

Figure 4.4.1: The spectrum of the LED around its maximum of 397 nm. On the x-axis only a cutout of 200 nm around the peak is shown. For an analysis of the reflectivity, a range of 387 nm to 411 nm can be used (ranged by the two blue, dashed lines).

4.5 Measurement Control using the Arduino

An Arduino Uno is a programmable microcontroller, used to control the whole experimental setup [19].

A circuit of the Arduino is presented in figure 4.5.1. In combination with an extension named "motor shield", the Arduino is able to drive a stepper motor. The stepper motor is bipolar stepper (ST2818M1006 Nema 11 from Nanotec Electronic) providing a single step of $(1.80 \pm 0.09)°$[20]. The wiring of the bipolar stepper is presented in figure 4.5.2. A gear box (GPLL 22-25 from Nanotec Electronic) divides one single step of the stepper into 25 intermediate steps with an efficiency of 70% [21].

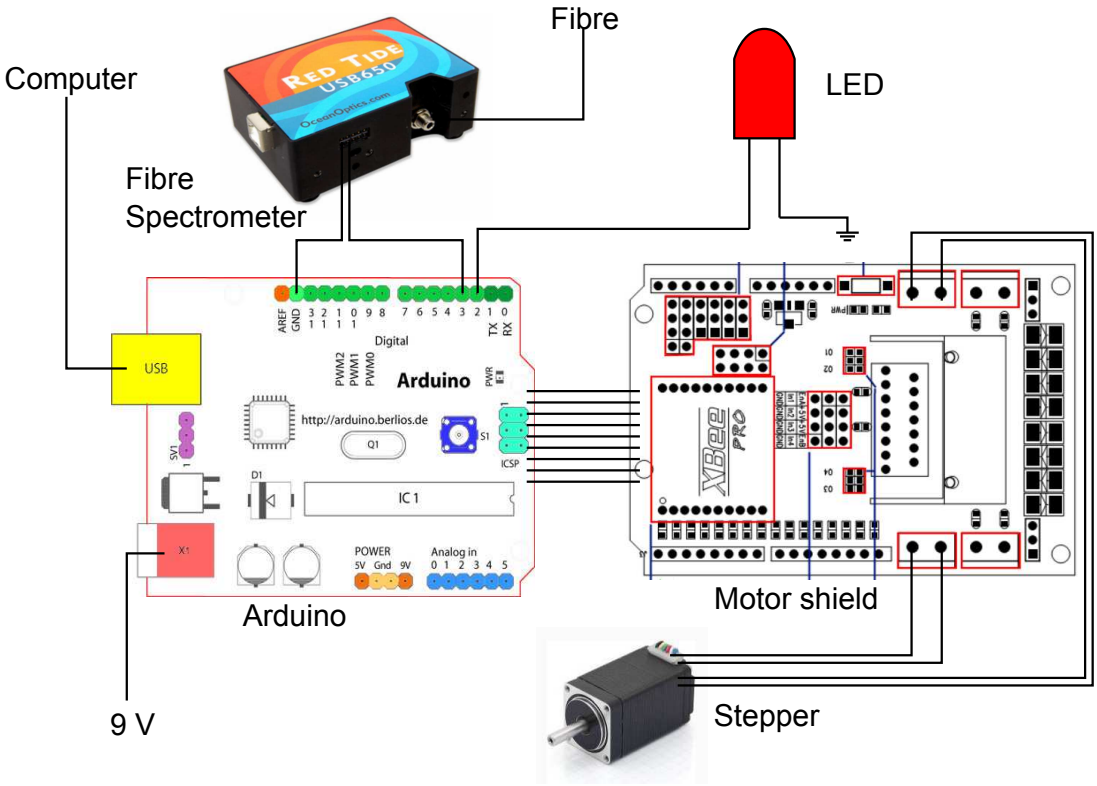

Figure 4.5.1: The circuit diagram of an Arduino: The Arduino is connected to the computer and an external power supply. The motor shield is plugged onto the Arduino and is connected to the LED, the stepper and the fibre spectrometer.

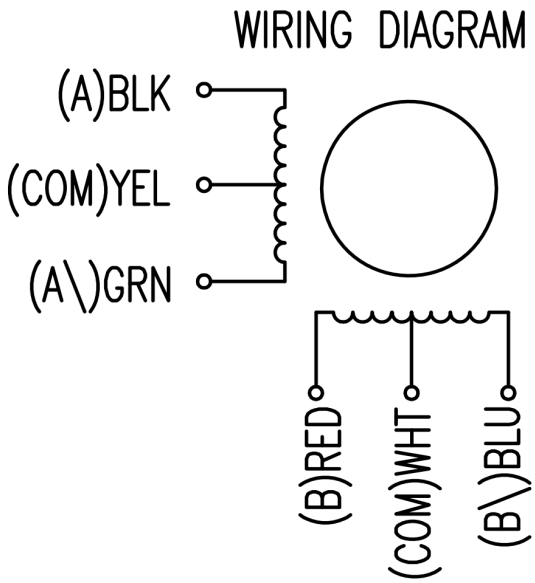

Figure 4.5.2: The wiring of a bipolar stepper. Two seperate electric circuits with each one coil drive the stepper. Taken from [20].

Chapter 5

Data Analysis

In the following chapter, the procedure and analysis of the measurements and the results in dependence on the incident angle, wavelength and the stage of oxidation are discussed. In the end, the implication for the Winston cone in the telescope FAMOUS is pointed out.

5.1 Procedure

Each measurement follows the same procedure of measuring, no matter if the reflected beam of the aluminium surface or just the light beam directly is to be recorded. Only the starting point of the detection fibre is a different one. The detection fibre is always driven nearby the position, the light beam is promised to be. After each single measurement, the fibre moves back to the starting position to guarantee reproducibility of the measurement.

After the detection fibre has been moved by the stepper to position (1), (2), (3) or (4) (c.f. figure 5.1.1), the measurement begins with the Arduino board applying a voltage of 5 V to the LED to turn on the light. The different starting positions are shown in figure 5.1.1. (1) refers to the starting position for an incident angle of 45°, (2) for an incident angle of 65° and (3) for 75°. Different incident angles, apart from the range between 45° and 75°, are not realisable as the fastening base for the aluminium cube blocks the movement of the stepper. For measuring the unreflected beam, the detection fibre has to be moved to the starting point (4). All different starting positions are equidistant in 200 steps = 14.4°, since one step of the stepper is equal to 0.072°. This makes it easier to reproduce the detection fibre position. Furthermore, no absolute calibration of the stepper angle is needed as the single measurements are shifted, so that the maxima of the beam profiles of the scans all meat at the same position.

At next, a 5 V signal from the Arduino board is sent as a trigger to the spectrometer to pin 7 (c.f. 4.3.2) for 10 ns so that now the spectrometer records the incoming light the detection fibre picks up. Due to hardware limitations, the integration time is fixed to 50 ms. After the spectrometer has transmitted the spectrum to the computer via USB, the software Spectrasuite automatically saves the spectrum onto the hard disk. A dead time of 100 ms later, in which the spectrometer saves the spectrum, the stepper together with the detection fibre moves three steps[1] further in clockwise direction

[1] This is a good compromise between a fast measurement and the resolution of the single measure points.

which is equal to an angular movement of

$$3\,\text{steps} \cdot \frac{1.8^\circ}{25}/step = 0,216^\circ.$$

Waiting a short time (100 ms) is necessary to damp the vibration of the stepper.

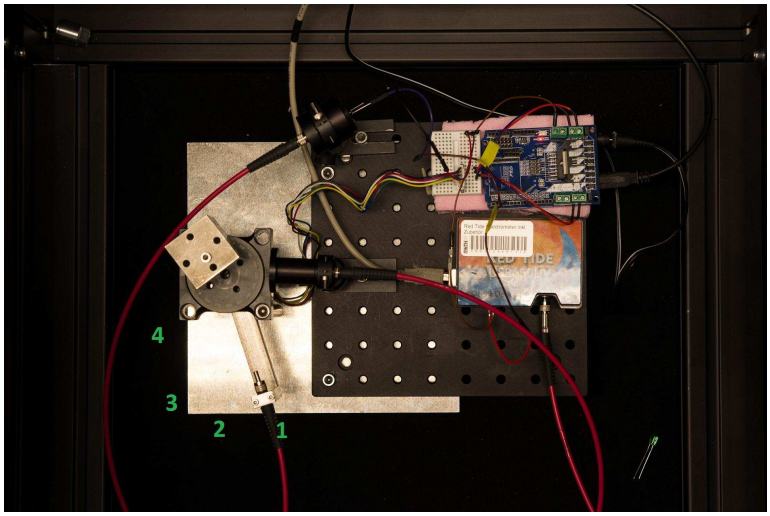

Figure 5.1.1: The experimental setup presented again, now with the different start positions of the detecting fibre: Measurement of the reflected beam at 45° (1), at 60° (2), at 75° (3). For measuring the unreflected beam (without the aluminium surface in the optical path), the detector starts at (4).

The measurement process is iterated 278 times. A spectrum is recorded, sent to the hard disk of the computer and so on. After 278 spectra were recorded and saved, the detection fibre is automatically moved back to the position at which the measurement has started. 278 movements of three steps at the gear box of the stepper correspond to a complete angular distance of 60°. During the whole measurement the LED stays turned on keep the light output as stable as possible.
Every measurement is repeated 8 times for the same set of parameters. Thus, a complete measurement includes eight times a record of spectra for each of the three different incident angles 45°, 60° and 75° and eight recorded spectra for the unreflected beam. Since one single measurement takes about two minutes, about half an hour is needed to carry out one complete measurement.

A measurement for an incident angle of 45° is presented in figure 5.1.2. It displays the enlargement of the light beam shifted to the maximum of the detected light located to $\Delta\Theta = \Theta - \Theta_0 = 0^\circ$. The angle displayed on the x axis refers to the angles, the stepper drives through[2]. The uncertainties of the x values correspond to the uncertainty of the stepper, the y axis uncertainties to the uncertainties of the number of counts N:

$$\sigma_N(\Theta) = \sqrt{N(\Delta\Theta)} \tag{5.1.1}$$

[2]This is not the incident angle, but the angular position of the stepper in relation to the maximum peak of the detected light beam.

The first of the 278 spectra is used as a dark spectrum reference, which is needed since the noise of the spectrometer is approximately 100 counts per 50 ms. All other spectra are subtracted by the dark spectrum. Thus, for the most angles presented in 5.1.2 the number of counts is equal to zero, so that only a short range around the maximum of a few degrees to the left and right has to be viewed. This plot corresponds to a wavelength of 397 nm. The enlargement of the reflected beam (green continuous line) compared to the unreflected beam is clearly visible. The impure surface has expanded the beam profile and has reduced the intensity of the beam.

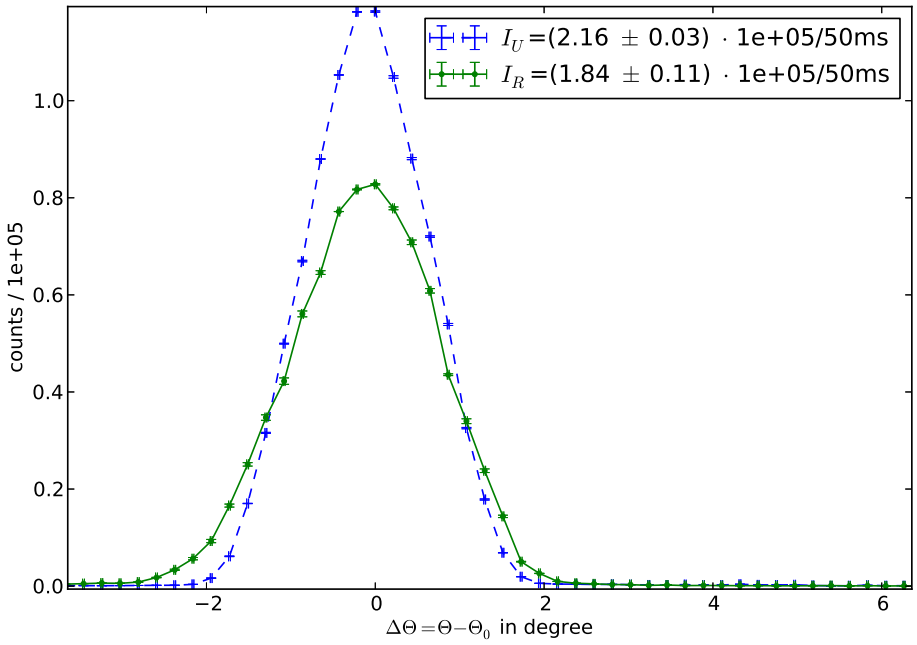

Figure 5.1.2: Exemplary plot of the measured intensity. It refers to an incident angle of 45° at a wavelength of 397 nm. The green line refers to the reflected beam and blue line to the unreflected one. The reflectivity is calculated to $(85.3 \pm 5.2\%)$.

The integral of the graph then leads directly to the intensity:

$$I = \frac{\int N(\Delta\Theta)\mathrm{d}\Delta\Theta}{t} \tag{5.1.2}$$

The integral is not calculated as a sum, instead a numerical method called Simpson's Rule is used to approximate the integral. The great advantage is, that the number of steps done between to records of a spectrum does not make any difference for the result. The single points of the graph can now be analysed as part of the Simpson's Rule's function f(x). Its integral then can be approximated by

$$\int_a^b f(x)\,dx \approx \frac{b-a}{6}\left[f(a) + 4f\left(\frac{a+b}{2}\right) + f(b)\right] \tag{5.1.3}$$

and is quadratic interpolation of a given function f(x)[22]. In this case the intensity then is approximated by

$$I_k(\Theta) = \sum_{j=0}^{138} \int_{-30+0.216\cdot j}^{-30+0.216\cdot(j+1)} N(\Delta\Theta)\mathrm{d}\Delta\Theta \approx \frac{0.532}{6}\left[N(0.216) + 4N(0) + N(-0.216)\right] \tag{5.1.4}$$

so that at the end a full angular range of 60° is passed through. All eight measurements for one configuration (wavelength, incident angle) are individually integrated with this Simpson's Rule and in the end the average is calculated:

$$I_{\mathrm{mean}} = \frac{1}{8}\sum_{k=1}^{8} I_k \tag{5.1.5}$$

The uncertainty of the average is gained via the uncertainty on average:

$$\sigma_{I_{\mathrm{mean}}} = \sqrt{\frac{1}{8-1}\sum_{k=1}^{8}(I_k - I_{\mathrm{mean}})^2} \tag{5.1.6}$$

This uncertainty dominates the uncertainties from every single measurement (accuracy of the stepper, histogram error of the counts) and is therefore the only one, that is considered for the following analysis.

5.2 Reflectivity Measurement

This chapter will concentrate on the analysis of the measured reflectivity in dependence on the different parameters wavelength and the incident angle. In the end, the influence of the results on the Geant4 simulation for the Winston cone is discussed.

5.2.1 Wavelength Dependence

To compare the wavelength dependent reflectivity for aluminium in different stages of oxidation, at five different times the light beams were detected. At first, the reflectivity of the polished aluminium is determined. After two, twelve and 20 days, new measurements were performed to get information on how the reflectivity might change during time. Another measurement with a humid surface should show whether there is any influence on the reflectivity characteristics.
The reflectivity is plotted in a new graph for every of the different stages of oxidation polished, two days, twelve days and 20 days of oxidation and for the humid surface. If values for the reflectivity are greater than 1.0, which is not a physical number for a reflectivity, they are reduced to a value of 1.0 with errorbars only downwards.

In figure 5.2.1 the reflectivity for different stages of oxidation for an incident angle of the light beam of 45° is presented. The blue solid line describes the reflectivity expectation from the Fresnel equations. It is useful to first compare the measured reflectivity with the expectation and second to compare the reflectivity in different stages of oxidation.

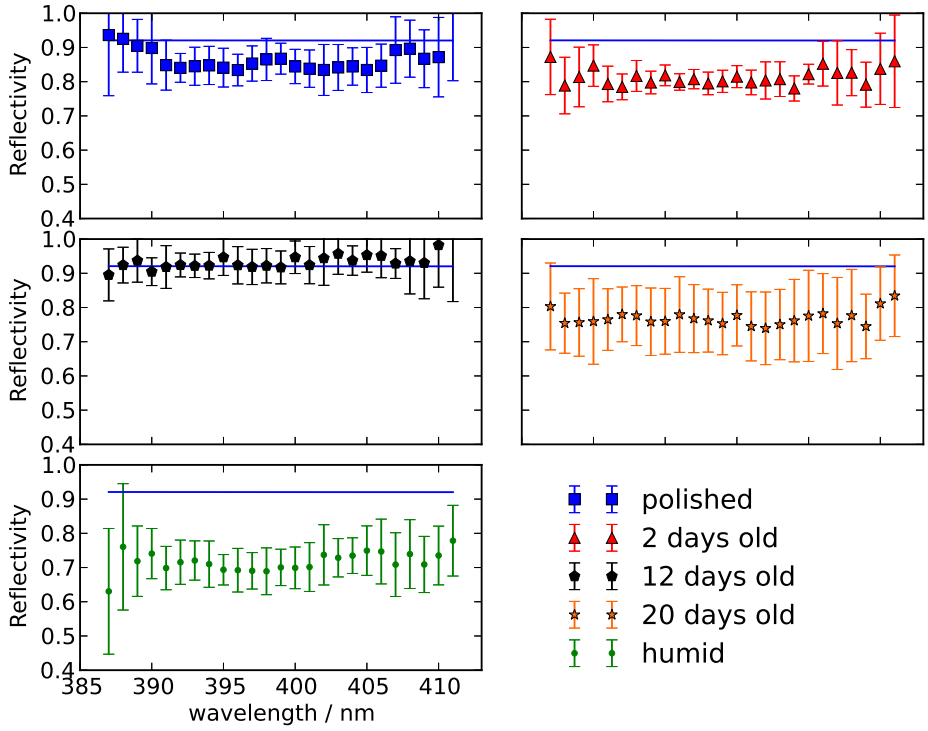

Figure 5.2.1: The wavelength dependent spectrum for a range between 387 nm and 411 nm. This measurement refers to an incident angle of 45°. The solid line in each subplot presents the expectation from the Fresnel equations.

Focussing on the reflectivity for the beam of polished aluminium (blue squares), the reflectivity stays stable over the whole wavelength range and nearly meets the expectation of the Fresnel equations. Only for the four smallest and greatest of the observed wavelength, the reflectivity fluctuates to higher values. In these borderland region, the absolute number of counts is already much less than around 400 nm (c.f. figure 4.4.1) and as a result also the corresponding errors on the reflectivity are higher. After two days of oxidation, the reflectivity has been measured again. The corresponding data is plotted by the red triangles. In nearly the whole wavelength range, the reflectivity is a little below the one concerning the polished aluminium, but within the uncertainties both reflectivity measurements are in agreement towards each other.
The measurements after twelve (black pentagons) and after twenty days (orange stars) also agree to the former data, although the reflectivity seems to be higher after twelve days of oxidation - even higher than the Fresnel expectation. But considering the errors, no tendency towards worse or even better reflectivity is clearly visible.

Measuring the reflectivity for a humid aluminium surface (small green dots), one can see first that for a wide range of wavelength the reflectivity falls to values of 0.7 and the error bars are far greater arising from stronger up- and downturns in the reflectivity in each of the eight measurements. A tendency for humid aluminium surfaces is discussed further downwards by describing the influence of the humidity at other incident angles.

In figure 5.2.2 the measured reflectivity for an incident angle of the light at 60° is plotted again for a polished aluminium surface, for a two, twelve and twenty days oxidised surface and for a humid surface.

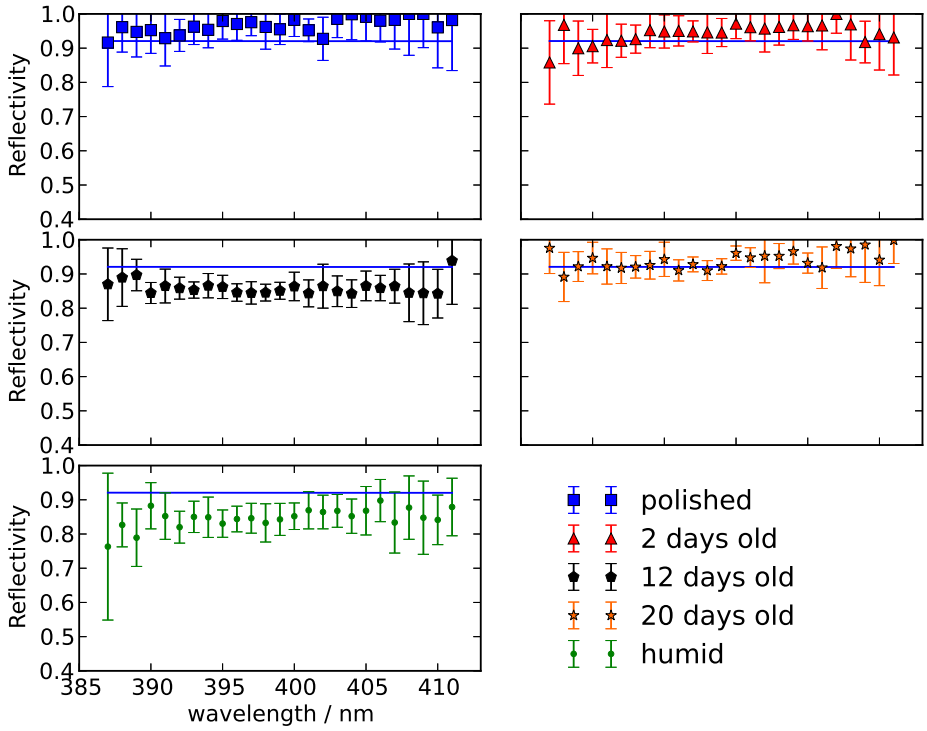

Figure 5.2.2: The wavelength dependent spectrum for a range between 387 nm and 411 nm. This measurement refers to an incident angle of 60°. The solid line in each subplot presents the expectation from the Fresnel equations.

The reflectivity for the polished aluminium surface (blue squares) indeed fluctuates over the wavelength range, but with no special tendency, as the error bars again are greater than the fluctuation of the single reflectivity measurements. The measurements for two days of oxidation (red triangles) fluctuate again and are not as stable on one distinctive reflectivity level as it was for 45°. Nevertheless, the values are again in the region of reflectivity as those of polished aluminium. After twelve days of oxidation the measured reflectivity decreases of an average of 8% to 10% (black pentagons). As after eight more days of oxidation (orange stars), the reflectivity again increases to the values of polished aluminium, the conclusion is close, that also for an incident angle of 60°, the reflectivity does not change during the oxidation process. For nearly all wavelengths,

the reflectivity is measured to a higher value than the Fresnel equations would expect - except for the twelve day oxide layer and for the humid aluminium surface. The decrease after twelve days of oxidation thus has to be reasoned differently. Possible explanations might be the state of different external parameters like the temperature or air moisture or pressure. The intensity of the LED is temperature dependent and thus the LED needs some time to warm-up after it is turned on.
For the humid surface, the reflectivity drops to fluctuating values around 0.85, which is indeed less than for the oxidised surface. Only the twelve days oxide layer corresponds to the humid surface which could be an evidence for a high air humidity at that day, the twelve day oxide layer was measured, has deteriorated the reflectivity.

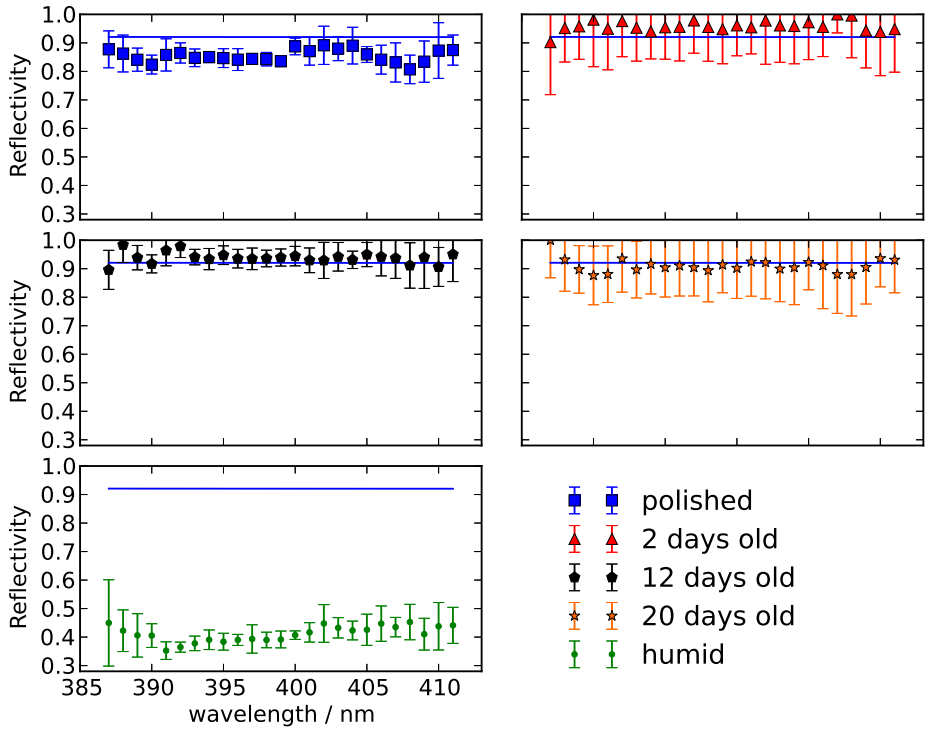

Figure 5.2.3: The wavelength dependent spectrum for a range between 387 nm and 411 nm. This measurement refers to an incident angle of 75°. The solid line in each subplot presents the expectation from the Fresnel equations.

For an incident angle of 75°, again five measurements at different stages of oxidation or in one case of humidity were performed. The results are presented in figure 5.2.3. The first data that really differs from the other plots is the really low reflectivity of the humid aluminium surface. For high incident angles humidity seems to get more problematic than it was the case for smaller ones.

The reflectivity for polished aluminium (blue squares) is approximately located around 0.85 with fluctuations up to 0.9 at the top and 0.8 at the bottom. Comparing the reflectivity for 2 days (red triangles), twelve days (black pentagons) and twenty days of oxidation (orange stars), the reflectivity is higher than for a polished aluminium sur-

face and thus even higher than expected from the Fresnel equations. However, strong fluctuations depending on the wavelength and high errorbars indicate the data to all different stages of oxidation to describe the same value of reflectivity and no clear tendency is visible, that the reflectivity changes during oxidation processes.

Concluding the analysis of the wavelength dependent reflectivity, one can say that there is no evidence for the oxidation layer on the aluminium surface to reduce the reflectivity. In case of the three different incident angles 45°, 60° and 75° the reflectivity stays around 90%. Fluctuations of single measurements that differ from this value, still correspond to the value of 90% due to high errors.
If the aluminium surface gets humid, this might cause reflectivity to partly decrease enormous, as it was presented for 75°.

5.2.2 Angular Dependence

As stated before, the reflectivity depends on the incident angle as already presented in figure 3.3.1. The angular dependence for a wavelength of 400 nm is plotted in figure 5.2.4. For an incident angle of 45°, the reflectivity is - with one exception -below the Fresnel expection. In contrast to that, the values of reflectivity for 60° and 75° are really scattered around the expectation.

The missing data especially for the humid surface at 75° is not plotted in this figure, because the value is far below 0.6.

5.3 Influence on the Winston Cone Operation

The reflectivity of the aluminium surface has direct influence on the efficiency of the whole FAMOUS telescope and especially on the detection of the silicon photomultiplier.

In figure 5.3.1 the fraction of the detected light as a function of the exit angle is presented. The difference between a 100% spike reflecting (blue) and for 100% lobe reflecting surface (red) occurs in both the angular distribution and the transmission. The lobed surface leads to a higher range of possible exit angles and the transmission decreases from 91% to 78%.

Therefore, a Geant4 simulation of the light flux as a function of the incident and exit angle of the Winston cone was made to recognise differences in the detected light flux efficiency. In figure 5.3.2 the distribution of the light flux as a function of the incident angle on the Winston cone is presented. The plot on the top refers to complete spike reflection, whereas the plot on the bottom describes the situation for fully lobe reflected light. The detection efficiency of the Winston-cone-SiPM-system is presented in blue colour code. The darker, the more efficient.

Comparing the two plots, one can see, that for a completely spiky surface, the efficiency is constant for incident angles up to 26° (which is the maximum incident angle, c.f. 2.5.2) for a light flux of up to 100 photons per ns.

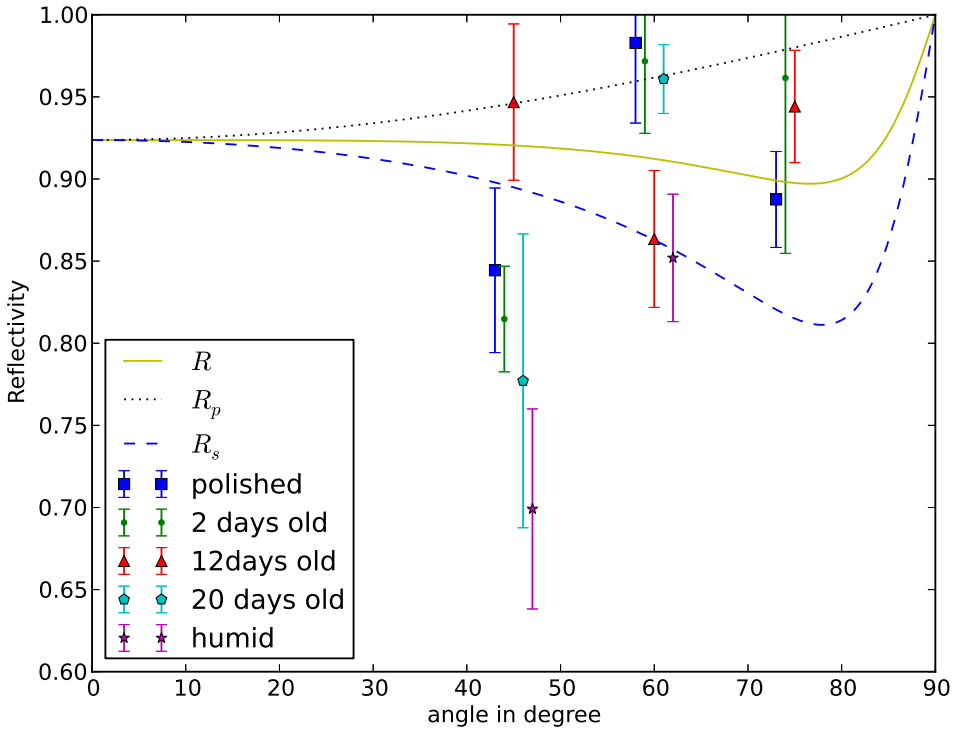

Figure 5.2.4: The angular dependence of the reflectivity. The data is a little shifted around the three incident angles of $45°$, $60°$ and $75°$ to better improve visibility on the x-axis.

In contrast to that, the detection efficiency for a surface with 100% lobe reflectivity has got a strong dependence on the incident angle. The highest efficiency is given for small incident angles and a small light flux and decreases strong for rising incident angles or a rising light flux. Furthermore the maximum detection efficiency with 0.18 is approximately 5% smaller than for spike reflected surfaces (up to 0.23).

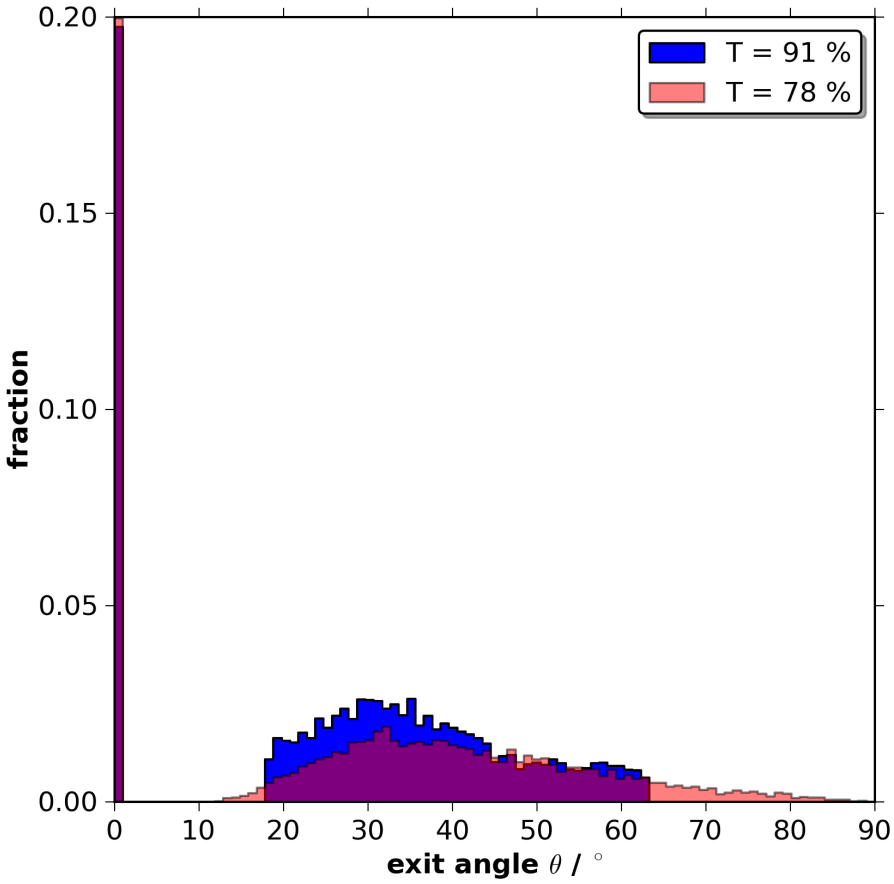

Figure 5.3.1: The angular distribution of a 100% spike reflecting (blue) and for 100% lobe reflecting surface (red). The lobe surface leads to a higher range of possible exit angles and transmission decreases.

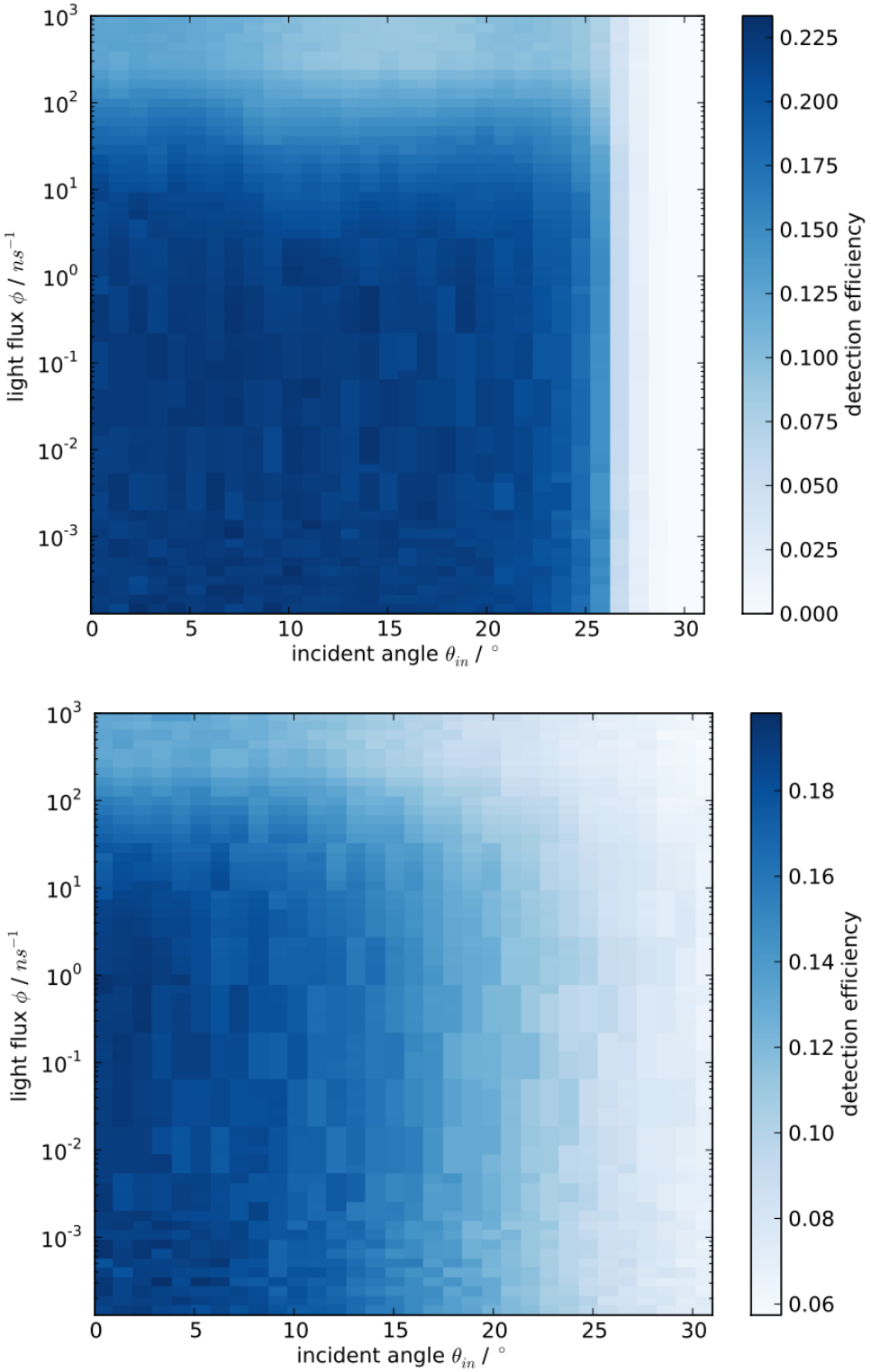

Figure 5.3.2: The Geant4 Simulation of the light flux efficiency of the Winston-Cone-SiPM-system. **Top:** The reflectivity of the Winston cone is set to 100% spike reflectivity. **Bottom:** The reflectivity of the Winston cone is set to 100% lobe reflection and σ_α is set to 12°

Chapter 6

Conclusion

The fluorescence telescope FAMOUS will consist of a refractive Fresnel lens with the diameter and the focal length $D = f = 510\,mm$. The focal plane consists of 64 single silicon photomultipliers aranged in a hexagonal structure. To increase the size of the focal plane and decrease dead space between the single SiPMs, Winston cones will be used as light funnels. They have got an entrance radius of $r_1 = 6.7\,mm$ and an exit radius of $r_2 = 3\,mm$. This causes the effective area increase by a factor of five.

The Winston cones are made of polished aluminium to have a high transmission. For a wavelength of 400 nm, the refractive index of aluminium is $\tilde{n} = n + i\kappa = 0.4879 + 4.8355i$. Making use of the Fresnel equations, the reflectivity for an unpolarised light source, hitting a plane, surface can be determined to be in a range between 0.9 and 0.95 in a wide range of incident angles. Impurities caused by oxidation processes can reduce the reflectivity to deteriorate and instead of just a spike reflection (the surface acts like a perfect mirror), lobe (the surface consists of small microfacets scattering the light to different directions) or Lambertian reflection (the reflectivity of the surface follows the Lambertian Law, which is principally a cosine function) can occur.

For the experimental setup, an LED in the UV region is used as a light source and a detection fibre connected to a fibre spectrometer is used to measure the intensity of the LED beam at a wavelength resolution of 1 nm.
First, the intensity of the light beam is measured. Secondly, the aluminium surface is positioned in the optical path to measure the intensity of the reflected light beam. The ratio of the intensities directly gives the value of reflectivity. It was determined to stay constantly at values between 0.7 and 0.95 depending on the different incident angles of 45°, 60° and 75° on the aluminium surface. The reflectivity was measured for different stages of oxidation of the aluminium - after two, twelve and 20 days, but no effect of a decreasing reflectivity was recognised within the resolution of the uncertainties. However, a humid surface does partially reduce the reflectivity enormously up to 30%.

Thus, even a long term use of the Winston cones in the FAMOUS telescope will not reduce the efficiency of the reflectivity properties of the aluminium surface. The Winston cones are now ready to be used in the telescope to enable measurements of first light at end of this year.

Bibliography

[1] Johannes Blümer, Ralph Engel, and Jörg R. Hörandel, "Cosmic Rays from the Knee to the Highest Energies," 2009.

[2] K. Nakamura et al. (Particle Data Group), "2011 Review of Particle Physics," *J. Phys. G 37*, 075021 (2010) and 2011 partial update for the 2012 edition.

[3] F. Arcipetre et al. *Nucl. Phys. Proc. Suppl. 150*, pp. 186–189, 2006.

[4] M. Ave et al. (AIRFLY Collab.) *Nucl. Instr. Meth. A 597*, p. 41, 2008.

[5] Tim Niggemann, "New Telescope Design with Silicon Photomultipliers for Fluorescence Light Detection of Extensive Air Showers," Master's thesis, 2012.

[6] Tim Niggemann, Thomas Hebbeker, Markus Lauscher, Christine Meurer, Lukas Middendorf, Johannes Schumacher & Maurice Stephan, "The Optics and Detector-Simulation of the Air Fluorescence Telescope FAMOUS for the Detection of Cosmic Rays," *SPIE*, vol. 8444.

[7] Maurice Stephan, Thomas Hebbeker, Markus Lauscher, Christine Meurer, Tim Niggemann & Johannes Schumacher, "Future use of silicon photomultipliers for the fluorescence detection of ultra-high-energy cosmic rays," *SPIE*, vol. 8155.

[8] Markus Lauscher, "Characterisation Studies of Silicon Photomultipliers for the Detection of Fluorescence Light from Extensive Air Showers," Master's thesis, 2012.

[9] Daniel Wilson, "Angular Dependence of the Relative Photon Detection Efficiency of Silicon Photomultipliers." to be published in September 2012.

[10] Wolfgang Demtröder, *Experimentalphysik 2 - Elektrizität und Optik*. Springer Verlag, 2004.

[11] "http://refractiveindex.info/?group=metals&material=aluminium," 05.09.2012.

[12] J.I. Larruquert, J.A. Mendez, J.A. Aznarez, "Far-UV reflectance of UHV-prepared Al films and its degradation after exposure to O2," *Applied Optics*, vol. 33, 1994.

[13] Minghong Yang, Alexandre Gatto, Norbert Kaiser, "Highly reflecting aluminum-protected optical coatings for the vacuum-ultraviolet spectral range," *Applied Optics*, vol. 45, 2006.

[14] "Physics 323, Lecture 16, Optics."

[15] "Polarisierte Lichtquelle (de 10 2007 053 297 .2) [0002]," 11 2007.

[16] Martin Janecek, William W. Moses, "Simulating Scintillator Light Collection Using Measured Optical Reflectance," 2010.

[17] Paloma Diaz, "Simulating light collection,"

[18] "www.oceanoptics.com/technical/usb2000%20operating%20instructions.pdf," 31.08.2012.

[19] "http://arduino.cc/en/main/arduinoboarduno," 09.09.2012.

[20] "http://de.nanotec.com/downloads/pdf/3724/st2818s1006%20layout1%20(1).pdf," 03.09.2012.

[21] "http://de.nanotec.com/downloads/pdf/3367/gpll22-gearbox+datenblatter%20layout1%20(1).pdf," 03.09.2012.

[22] "http://mathworld.wolfram.com/simpsonsrule.html," 05.09.2012.

Acknowledgements
Danksagungen

Hier möchte ich mich bei allen Leuten bedanken, die mich bei dem Erstellen dieser Arbeit unterstützt und dabei begleitet haben. Es ist unmöglich, allen Leuten hier persönlich zu danken. Daher danke ich auch all denen, die mir während der Anfertigung meiner Bachelorarbeit geholfen haben, aber nicht namentlich erwähnt werden.

Besonderen Dank gilt es vor allem an Herrn Prof. Dr. Hebbeker zu richten, der es mir überhaupt erst ermöglicht hat, diese Bachelorarbeit an seinem Institut und unter seiner Leitung anzufertigen. Vielen Dank dafür.

Des Weiteren möchte ich mich bei meinem Betreuer Tim Niggemann bedanken, der mich in endlosen Stunden unterstützt hat, von der Ausarbeitung eines Experimentierablaufs bis hin zur fertigen Bachelorarbeit zu gelangen und mir immer wieder mit wertvollen Tips sowie Hilfestellungen zur Seite stand. Ohne dich hätte ich gerade im Einstieg in die mir komplett neue Programmiersprache Python große Probleme bekommen. Herrn Dr. Markus Merschmeyer danke ich für seine Geduld, wenn ich zum wiederholten Male zum gleichen Thema seine Hilfe in Anspruch nehmen musste.

Ich bedanke mich auch bei allen Mitarbeitern der Auger-Arbeitsgruppe, die mir in wöchentlichen Meetings neue Ideen und Anstöße gegeben haben, um mich weiter mit der Materie auseinanderzusetzen und von anderen Gesichtspunkten zu betrachten. Insbesondere möchte ich mich dabei bei den Mitarbeitern unserer FAMOUS-Kollaboration bedanken, neben Tim Niggemann bestehend aus Christine Peters, Maurice Stephan, Markus Lauscher, Rebecca Meißner und Daniel Wilson.

Großen Dank gilt an die Mitarbeiter der Institutswerkstatt, die mir meinen Messaufbau gebaut haben und immer geholfen haben, als ich Materialien brauchte oder die Aluminiumoberfläche neu poliert haben musste. Besonders möchte ich Herrn Barthel Philipps meinen Dank ausdrücken für die Konstruktion des Messaufbaus sowie das schnelle Umsetzen von spontanten Änderungen am Aufbau.

Zu guter Letzt danke ich meiner Familie und Freunde für den guten Rückhalt und die mentale Unterstützung während meiner Bachelorarbeit.

Erklärung

Ich versichere, dass ich die Arbeit selbstständig verfasst und keine anderen als die angegebenen Quellen und Hilfsmittel benutzt habe. Alle Stellen, die dem Wortlaut oder Sinn nach anderen Quellen entnommen sind, habe ich in jedem einzelnen Fall unter genauer Angabe dieser deutlich als Entlehnung kenntlich gemacht.

Aachen, den 13.9 .2012

Sebastian Mann